IEEE Transaction on Transportation Electrification

PV-Integrated Auxiliary Power Module Using Hybrid Multi-Input Multi-Output DC-DC Converter for Electric Vehicle Applications

Majid Mehrasa, *Senior Member, IEEE*, Naser Vosoughi Kurdkandi. *Member, IEEE*, and Chunting Chris Mi., *Fellow, IEEE*

***Abstract*— This paper proposes a hybrid multi-input multi-output DC-DC converter for integrating Photovoltaic (PV) unit and auxiliary power module (APM) to simultaneously supply low voltage/power loads inside electric vehicle (EV) as well as actively participate in EV battery management system (BMS). Defining three operation modes including charging, discharging and idle, the proposed converter guarantees multiple outputs isolated from EV-high voltage battery (EV-HVB) with significant safe operation regardless of the power flow direction between the auxiliary battery and EV battery cell. Compared to the existing APMs, the proposed PV-integrated APM provides much wider voltage ranges for internal loads based on low voltage auxiliary battery (LVAB) with a smaller voltage rate and size. Using pole placement method (PPM) as well as comprehensive large-signal and small-signal dynamic models, two closed-loop control systems are presented to enable the desirable current flow and regulated output voltages. To this end, the controllability of the proposed system is extensively assessed, and the effective state feedback gains are designed associated with the closed-loop system eigenvalues with the adjusted and sufficient stability margin. Both simulation and experimental results are employed to verify the noticeable contribution of proposed system along with the designed control technique to APM and BMS in EV applications.**

***Index Terms*— Auxiliary power module, battery management system, PV integration, hybrid DC-DC converter, electric vehicle, high voltage battery cell.**

I. INTRODUCTION

A very well-designed APM system is considered as a significant advantage of EVs for reaching the functional features such as high efficiency, safety and reliability, integration capability, compact design, modularity and scalability. In this regard, researchers and industries have attempted to design appropriate APM systems through meeting the features mentioned above. To this end, some works focused on interfaced-power electronic converters (PECs) between EV-HVB and LVAB [1], by designing active filter auxiliary power module [2], all-in-one magnetic integrated structure of phase-shift full-bridge current doubler converter (PSFB-CDC) [3], and high-frequency high power density PSFB-CDC [4]. Using active power decoupling (APD) technique and full-bridge single-phase dual active bridge (FBSP-DAB) converter with soft switching capability, the charging configuration of the auxiliary battery in the EV driving charging mode was made in [5]. In [6], to eliminate the low-frequency harmonic currents in the high-voltage battery (HVB) charger when the HVB is charging, the LVAB and EV-HVB were connected to each other using integrated active filter APM converter based on dual-voltage charging systems. A two-stage bidirectional design including interleaved buck DC-DC converters and DCX (dc transformer based on series-input parallel-output FBSP-DAB) was proposed in [7] to provide a wide operating voltage range, e.g., 250–450 V for EV-HVB and the high-voltage 10–16 V at the LVAB. Moreover, [8] presented a reconfigurable current-fed dual active bridge (CFDAB)-based converter for ultrawide APM applications with the input voltage from 180 to 900 V and an output voltage from 6 to 16 V. Also, a three-tasks onboard charger (OBC) including a selective switch, a high-frequency transformer, and inductors was proposed in [9] to separately charge the battery of plug-in electric vehicles (PEVs), act as an inverter, and charge LVAB using PEV battery as a step-down converter in the driving operation mode.

Some other works directly employed wireless power transfer (WPT) concept and multi-winding transformers for making stable LVAB [10-11]. In [12], an APM full-bridge single-phase converter with transformer was exerted for the LV regulation and the LV/HV output isolation, while the doubled-sided single-phase DAB LCC topology based on WPT was considered for the HV battery. As another related work to integrate the OBC, WPT, and APM in one unit, a multi-winding WPT-based magnetic connection was developed in [13] to remove the main transformer of OBC and APM. On the other hand, the HV and LV batteries were able to be simultaneously charged based on the integration of OBC and APM through an isolated three-port dc–dc converter [14], wherein a three-winding transformer was designed to make galvanic isolation between the converter ports. It is worth mentioning that the bidirectional DC-DC converters used for actively balancing the EV-HVB cells (EV-HVBCs) were also adjusted as another solution for providing regulated LV by elimination of a separate HV-to-LV battery step-down DC–DC converter [15-16].

(Corresponding author: mmehrasa@uno.edu).

Majid Mehrasa is with the Department of Electrical and Computer Engineering, The University of New Orleans (UNO), 2000 Lakeshore Dr, New Orleans, LA, 70148, USA (e-mail: mmehrasa@uno.edu).

Naser Vosoughi Kurdkandi and Chunting Chris Mi are with the Department of Electrical and Computer Engineering, San Diego State University (SDSU), San Diego, CA 92182 USA (e-mail: nvosoughikurdkandi@sdsu.edu, cmi@sdsu.edu).

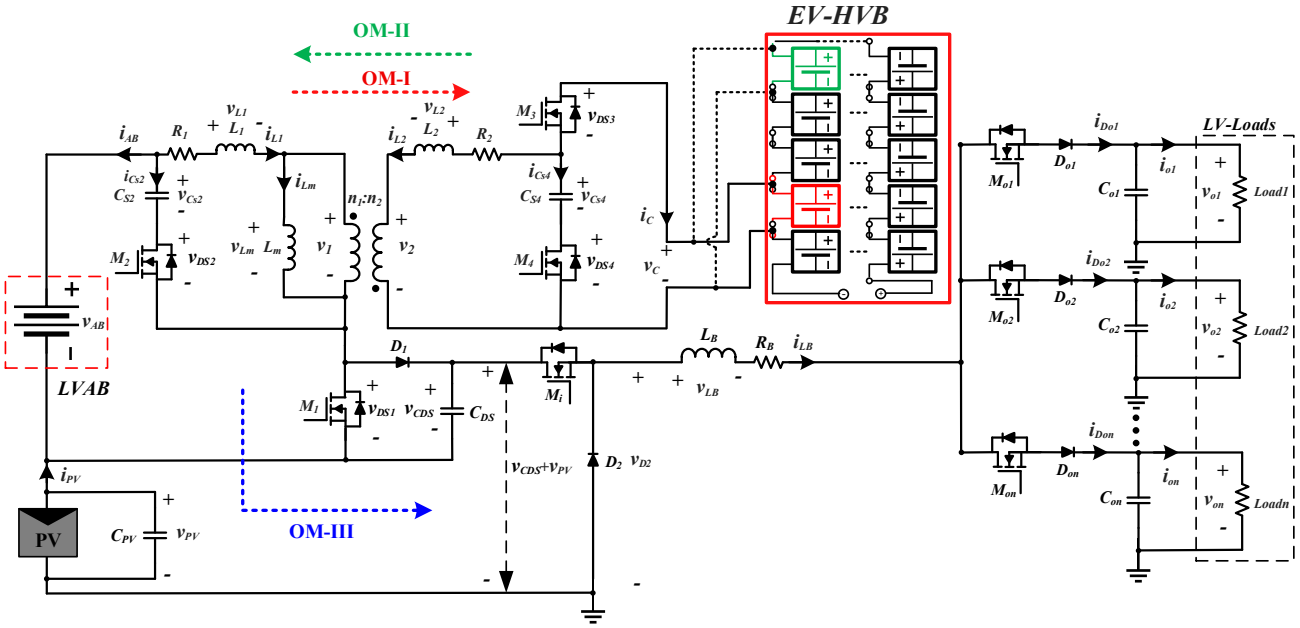

Fig. 1. Proposed PV-integrated APM and EV BMS using hybrid multi-input multi-output DC-DC converter.

For instance, a half-full bridge dual active bridge (HFB-DAB) DC-DC converter was proposed in [17] to combine the functionalities of a battery balancer and APM in which two HV battery cells were connected to the applied HFB-DAB DC-DC converter. The converter in [17] was changed to a dual-active half bridge (DAHB) DC-DC converter with coreless transformer for isolation and energy transfer in [18] to simultaneously enforce two EV-HVBCs for enabling the battery-balancing APMs as well. Also, using FBSP-DAB connected to the EV-HVBCs for persistent active cell balancing process, [19] could provide the required current of auxiliary loads commensurate with the state-of-charge (SOC) and capacities of the battery cells. The LV loads (LVLs) inside EVs should be supplied using appropriate structure of multiport DC-DC converter considering the voltage levels of auxiliary loads and connection between the EV-HVB and LVAB [20]. In [21], an integrated multiple independent-regulated-output buck converter with synchronous operation was proposed to simultaneously supply multiple LVLs. To fulfill the EV load demand, a 48V multiple-voltage bus converter with dual 12V dual supply system and additional flexible dc bus voltages was designed in [22]. Researchers have persistently tried to propose an effective multiport DC-DC converter for supplying EV auxiliary loads such as multi-input multi-output DC-DC converter with step-up capability [23], and single-input multi-output DC-DC converter without limitation regarding duty cycles and inductor currents [24], however, the works mentioned above don't have the advantage of concurrent contribution to EV-HVB BMS.

Meanwhile, a number of promising alternative concepts and approaches has recently emerged, focusing on the integration of photovoltaic panels within EV battery systems to increase driving range and achieve more efficient power utilization [25–26]. In this regard, some research works discussed the driving distance and environmental benefits [27-28], the route planning [29], the temperature rise of PV modules [30], and the high-efficiency solar cells [31]. By relying on solar battery packs, the photovoltaic vehicles presented in [32] and the solar-assisted electric vehicles described in [33] tackled the key challenges, including low energy utilization, high cost, and limited driving range. PV auxiliary power for battery electric buses has been developed to operate during in-motion and parking periods, thereby addressing vehicle scheduling challenges in solar electric bus systems [34]. Using wireless power transfer units and supercapacitor-based energy storage, a portable auxiliary photovoltaic power system was proposed for electric vehicles, incorporating a foldable scissor-mechanism concept [35]. In [36], the battery module with the lowest state of charge (SOC) in a solar power–assisted EV was charged using solar energy during vehicle driving, while energy losses were minimized through EV battery balancing by transferring solar and stored energy to the storage cell. In a PV-assisted EV, an onboard PV system was developed and integrated with a bidirectional charger, an auxiliary power module (APM), and vehicle-to-grid (V2G) applications [37]. As an on-board fuel, PV-based auxiliary energy source was investigated in distinct types of electrified vehicles including plug-in hybrid electric vehicles (PHEVs), full hybrid electric vehicles (FHEVs), and battery electric vehicles (BEVs) [38]. Only a few studies have somewhat outlined partial structures of power electronic converters for PV-assisted EVs, considering the multiple roles of PV systems, such as APM, BMS, and EV-HVB charging. In [39], one port of a multiport current-fed quad-active bridge converter was used for solar PV system that is connected to APM through a buck-boost DC-DC converter. The DC–DC converter topologies, including the unidirectional flyback, LLC resonant, and DAB converters, are employed in [40] to transfer power from the solar PV module to the LV battery.

Table I. Comparison of the proposed converter with previously presented APMs, both with and without integrated PV units.

		NoSs	NoDs	NoCs	NoIs	Nx	CSD	Efficiency (Max)	MSSs	IPVU	CTBMS	CTLVLs	CLVB
Proposed Converter	**APM-loads**	3	4	3	1	$1.5+v_{pv}/v_{Au}$ *to* $3+v_{pv}/v_{Au}$	Yes	94.5	$v_{cds}+v_{PV}$	Yes	Yes	Yes	Yes
	BMS	4	0	2	0								
[2]		8	0	3	2	NR	Yes	91	v_{HVB}	No	No	No	Yes
[3]		6	0	1	4	NR	No	95.5	v_{Au}	No	No	No	Yes
[5]		10	0	2	2	NR	Yes	96.95	v_{HVB}	No	No	No	Yes
[6]		8	0	3	4	NR	Yes	95.5	v_{HVB}	No	No	No	Yes
[7]		12	0	4	3	NR	Yes	96	v_{HVB}	No	No	No	Yes
[8]		10	0	4	5	NR	Yes	97	v_{HVB}	No	No	No	Yes
[10]		4	0	2	1	NR	Yes	92.6	v_{HVB}	No	No	No	Yes
[17]		b*6	0	b*3	b*1	NR	Yes	89.1	v_{Au}	No	Yes	No	Yes
[18]		b*4	0	b*3	b*2	NR	No	80	v_{Au}	No	Yes	No	Yes
[19]		b*8	0	b*3	b*1	NR	Yes	93	v_{Au}	No	Yes	No	Yes
[20]		2	2	2	2	1	Yes	94	v_{Au}	No	No	Yes	No
[21]		3	0	2	2	1	Yes	92.2	v_{Au}	No	No	Yes	No
[23]		5	5	5	4	NR	Yes	94.7	NR	No	No	Yes	No
[24]		2	2	2	2	1	Yes	94	v_{Au}	No	No	Yes	No
[36]		2	2	3	2	NR	Yes	95	$(1+a)v_{HVB}$	Yes	Yes	No	No
[39]		2	0	1	1	NR	Yes	NR	v_{PV}	Yes	No	No	No
[40]		1	1	2	1	NR	NR	NR	v_{PV}	Yes	No	No	Yes
		8	0	3	2	NR	NR	NR	v_{Au}	Yes	No	No	Yes
		8	0	2	2	NR	NR	NR	v_{Au}	Yes	No	No	Yes
[41]		1	2	4	2	NR	Yes	91.2	v_{PV}	Yes	No	No	No
[42]		7	0	9	2	NR	Yes	95.5	v_{HVB}	Yes	No	No	Yes
[43]		4	4	2	1	v_{PV}/v_{Au} *or* *1*	Yes	NR	v_{Au}	Yes	No	Yes	No

In a plug-in hybrid EV, the internal combustion engine was replaced by renewable energies wherein PV module injected power into the EV drive DC-link using unidirectional flyback converter [41]. As an interface between HVB/PV and LVB, [42] employed a phase-shifted, full-bridge DC-DC and buck converters to charge LVB from HVB and PV at the same time. A non-isolated multi-port DC-DC converter including two inputs/outputs with additional design details is presented in [43], enabling the injection of PV power into various loads within electric vehicles such as EV drive and low-rated loads. Given the research gaps identified in the above references, this paper proposes, for the first time, a hybrid multi-input multi-output DC–DC converter with an accurate dynamic model and an effective PPM to integrate the PV unit and APM for simultaneously supplying low-voltage/low-power loads inside electric vehicles and actively participating in the EV battery management system (BMS).The main contributions of the manuscript are 1) the proposed converter is capable of concurrently being a part of EV BMS and integrated APM to reserve the energy of EV-high voltage battery cells (EV-HVBCs) inside the auxiliary battery instead of dissipating the excess charge OR charge the EV-HVBCs using proposed APM system, 2) in each operation mode, the proposed DC-DC converter can always guarantee "n" outputs isolated from the EV-HVB regardless of the power flow direction between the auxiliary battery and EV battery cell. The "n" stands for the number of LVLs connected to SISIMO DC/DC converter, 3) This is the first time ever that an APM system can be involved with both PV unit power and BMS at the same time, 4) proposed APM system can provide load voltages larger than the LVAB rate with high efficiency. This feature enables the proposed APM system to utilize LVAB with a smaller voltage rate and size, and 5) A newly developed set of dynamic models, together with the applied closed-loop pole placement method provide the desirable current flow and regulated output voltages for all parts of proposed PV-integrated APM and EV-BMS. This paper is organized as follows. Introduction is presented in Section I. Section II focuses on explaining the proposed PV-integrated APM and EV-BMS along with their related dynamic large-signal models. Proposed control technique is discussed in Section III. This section includes two subsections detailing the controllability evaluation and the closed-loop control systems. Experimental results are provided in Section IV. Conclusion is given in Section V.

II. Proposed PV-integrated APM and EV BMS

Fig. 1 shows the proposed PV-integrated APM involved with BMS using a hybrid DC-DC Converter for EV applications. The hybrid converter consists of one active-clamped bidirectional flyback DC/DC converter (ACBFC) and one single-input single-inductor multi-output (SISIMO) buck DC/DC converter. The ACBFC provides one isolated output based on the power flow direction between LV auxiliary battery (LVAB) and EV high-voltage battery cells (EV-HVBCs). The isolated output will function as a part of BMS to store the energy of EV-HVBCs inside LVAB instead of dissipating the excess charge OR charge EV-HVBCs if applicable. On the other hand, the filtered voltage of v_{DSl} through the capacitor of C_{DS} (i.e., v_{CDS}) along with the PV voltage (i.e., v_{PV}) are assigned as the input of SISIMO buck DC/DC converter as depicted in Fig. 1. Given the charging/discharging conditions of low and high voltages, ACBFC will be adjusted to operate at three modes. Three color-coded dotted arrows are used to clearly illustrate the

three operating modes in Fig. 1. The fundamental operating waveforms, along with the corresponding gate signals, have been included for all operating modes as shown in Fig. 2.

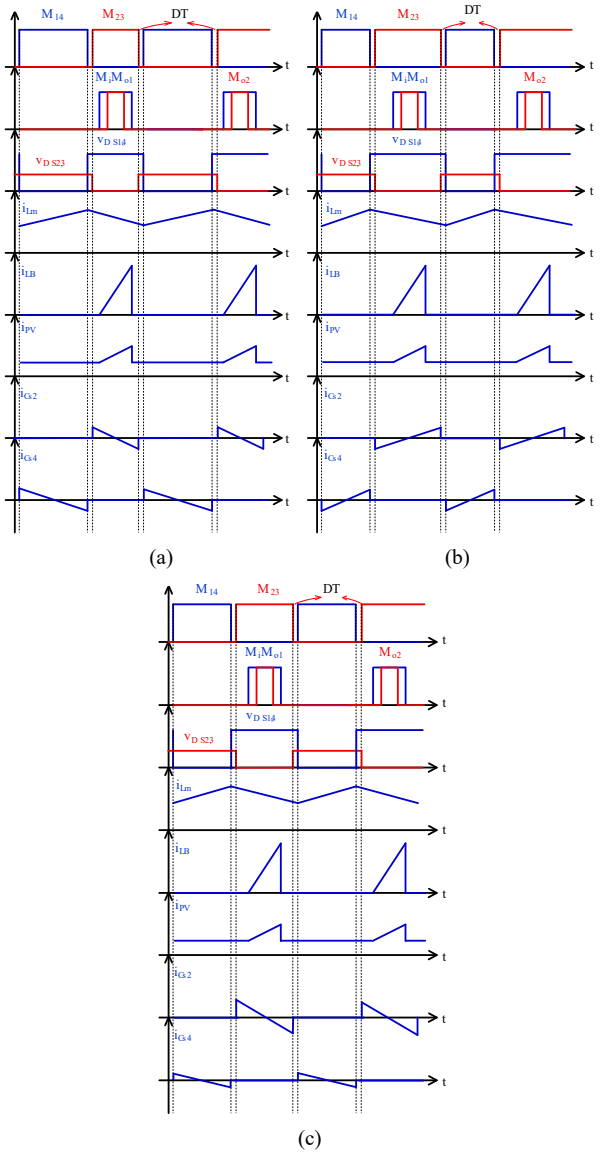

Fig. 2. Three operating modes of proposed converter (a) OM-I, (b) OM-II, and (c) OM-III.

In the first operation mode (OM-I), LVAB charges EV-HVBCs using the flyback converter leading to two inputs of $\{v_{AB}, v_{PV}\}$ and "$n+1$" isolated outputs (v_C, $v_{o1},\ldots,v_{on}$). The second operation mode (OM-II) makes the power flow direction from EV-HVBC to LVAB. The inputs of proposed converter in this mode are $\{v_{PV}$ and $v_C\}$ and also the converter will comprise "n" outputs ($v_{o1},\ldots,v_{on}$) isolated from the EV-HVB. In the last operation mode (OM-III), EV-HVBCs no longer need to be charged/discharged, and the low voltage loads (LVLs) are supplied through LVAB (v_{DSI}) and PV panel (v_{PV}). In addition, Table I is presented to accomplish a detailed comparison between the proposed PV-integrated APM and other reported APMs, both with and without PV units. In this table, the comparison has included number of switches (NoSs), number of Diodes (NoDs), number of capacitors (NoCs), the input voltage of LVLs over LVAB (Nx), the control system designed (CSD), maximum efficiency, maximum stress on switch (MSS), included PV unit (IPVU), contribution to battery management system (CTBMS), contribution to low voltage loads (CTLVLs), and contribution to low voltage battery (CTLVB). In this Table, "n" stands for the number of power converters used in the BMS-related APMs introduced in [17], [18], and [19]. Also, "a" should be satisfied in inequality $0 < a < 1$. As can be realized from Table I, among the PV-integrated APM configurations, the proposed converter is the only topology capable of simultaneously supporting the BMS, LVLs, and the auxiliary battery. Moreover, the proposed converter can achieve load voltages significantly higher than the LVAB—approximately between $1.5+v_{pv}/v_{Au}$ and $3+v_{pv}/v_{Au}$ times the auxiliary voltage level—further demonstrating its superiority over the other configurations discussed in Table I.

A. Proposed dynamic model

This section focuses on the dynamic models of ACBFC and SISIMO DC-DC buck converter used in the proposed system shown in Fig. 1. These dynamic models are employed for designing the proposed control systems enabling the hybrid converter to simultaneously function as APM and EV BMS.

A.1 Dynamic model of ACBFC

In ACBFC, when the switches of M_1 and M_4 are ON, the other switches of M_2 and M_3 are OFF, and vice versa. Given these switching states and three operation modes defined above, two duty cycles of the d_{m1} and d_{m2} are proposed for the switch M_1 to effectively control the currents of i_{Lm} and i_{L2}, respectively. Therefore, considering the voltages of LVAB (v_{AB}), EV-HVBC (v_c), and clamped capacitors (v_{cs2}, v_{cs4}), the dynamic model of ACBFC is equal to,

$$\frac{d}{dt}\begin{bmatrix} i_{Lm} \\ i_{L2} \end{bmatrix} = \begin{bmatrix} \dfrac{-(R_1)}{L_1+L_m} & 0 \\ \dfrac{-n(L_m R_1)}{L_2(L_1+L_m)} & \dfrac{-R_2}{L_2} \end{bmatrix}\begin{bmatrix} i_{Lm} \\ i_{L2} \end{bmatrix} + \begin{bmatrix} \dfrac{v_{AB}-v_{Cs2}}{L_1+L_m} & 0 \\ 0 & \left(-\dfrac{nL_m v_{Cs2}}{L_2(L_1+L_m)}+\dfrac{v_{Cs4}}{L_2}\right) \\ & \left(+\dfrac{nL_m v_{AB}}{L_2(L_1+L_m)}-\dfrac{v_c}{L_2}\right) \end{bmatrix}\begin{bmatrix} d_{m1} \\ d_{m2} \end{bmatrix} + \begin{bmatrix} \dfrac{v_{Cs2}}{(L_1+L_m)} \\ \dfrac{nL_m v_{Cs2}}{L_2(L_1+L_m)}+\dfrac{v_c}{L_2} \end{bmatrix} \quad (1)$$

In a well-designed control system, the relationship $D_{m1}=D_{m2}$ should be satisfied. D_{mi} (i=1,2) stands for the steady-state term of d_{mi}. Defining $\alpha=V_{AB}-V_{Cs2}$ and $\beta=n\alpha L_m + (L_1+L_m)(V_{Cs4} - V_c)$, the steady-state equality between the currents of L_m and L_2 in ACBFC is as follows:

$$I_{Lm} = \frac{\alpha(L_1+L_m)(R_2 I_{L2}-V_c)+(\beta-\alpha n L_m)V_{Cs2}}{\left[(R_1)\beta - n\alpha(L_m R_1)\right]} \quad (2)$$

Where V_x (x=c, $cs2$, AB, $cs4$), I_{L2}, and I_{Lm} are the steady-state values of *ACBFC* state variables shown in Fig. 1. As can be realized from (2), the steady-state values of both currents are affected by the voltage steady-state values of *EV-HVBC*, *LVAB* and clamped capacitors.

A.2 Dynamic model of SISIMO DC/DC Buck Converter

SISIMO Buck DC/DC Converter is responsible for supplying LVLs with different voltage levels. In this converter, the desired output v_{ok} ($k=1,\ldots,n$) for the LVL k^{th} is generated by appropriately providing the duty cycles d_{ok} and d_k aiming to control the switches M_i and M_{ok}, respectively. According to Fig. 1, the current i_{Dok} can emerge to the inductor L_B current using current division method leading to the following dynamic model for the buck converter,

$$\frac{d}{dt}\begin{bmatrix} v_{o1} \\ i_{Do1} \\ \ldots \\ v_{on} \\ i_{Don} \end{bmatrix} = \begin{bmatrix} \frac{-1}{R_{o1}C_{o1}} & \frac{d_{o1}}{C_{o1}} & 0 & 0 & 0 \\ \frac{-R_{p1}d_{o1}}{L_B} & \frac{-R_B d_{o1}}{L_B} & 0 & 0 & 0 \\ \ldots & \ldots & \ldots & \ldots & \ldots \\ 0 & 0 & 0 & \frac{-1}{R_{on}C_{on}} & \frac{d_{on}}{C_{on}} \\ 0 & 0 & 0 & \frac{-R_{pn}d_{on}}{L_B} & \frac{-R_B d_{on}}{L_B} \end{bmatrix} \begin{bmatrix} v_{o1} \\ i_{Do1} \\ \ldots \\ v_{on} \\ i_{Don} \end{bmatrix} + \begin{bmatrix} 0 \\ \frac{R_{p1}\left(v_{CDS}+v_{PV}\right)}{L_B} d_{o1} d_i \\ \ldots \\ 0 \\ \frac{R_{pn}\left(v_{CDS}+v_{PV}\right)}{L_B} d_{on} d_i \end{bmatrix} \tag{3}$$

Where $R_{pk} = -\left(R_{og} \| \ldots \| R_{om}\right)\left(R_{ok} + \left(R_{og} \| \ldots \| R_{om}\right)\right)^{-1}$ and $\{g,m\} \neq k$.

Based on the dynamic model of (3), the steady-state values of the duty cycles d_{ok} and d_i are obtained as the following,

$$D_{ok} = \frac{R_B V_{ok}}{R_{ok}\left(D_i R_{pk}\left(V_{CDS}+V_{PV}\right) - R_{pk}V_{ok}\right)} \tag{4}$$

$$D_i = \frac{R_B I_{Dok} + R_{pk} V_{ok}}{R_{pk}\left(V_{CDS}+V_{PV}\right)} \tag{5}$$

In the proposed hybrid converter, it is assumed that D_i is equal to the output duty cycle with the most value meaning that $D_i = D_{ok} + \Delta D_{ok}$ wherein $\Delta D_{ok} \geq 0$. "k" stands for k^{th} output duty cycle that does not have the maximum value. Substituting $D_{ok} = D_i - \Delta D_{ok}$ into (4), the k^{th} steady-state output duty cycle of SISIMO buck DC/DC converter is equal to,

$$D_{ok} = 0.5 f_1\left(\Delta D_{ok}\right) - \sqrt{0.25\left(f_1\left(\Delta D_{ok}\right)\right)^2 - f_2\left(\Delta D_{ok}\right)} - \Delta D_{ok} \tag{6}$$

Where,

$$f_1\left(\Delta D_{ok}\right) = \frac{V_{ok}}{V_{CDS}+V_{PV}} + \Delta D_{ok}$$
$$f_2\left(\Delta D_{ok}\right) = \frac{R_{ok}R_{pk}V_{ok}\Delta D_{ok} - R_B V_{ok}}{R_{pk}R_{ok}\left(V_{CDS}+V_{PV}\right)} \tag{7}$$

The relationship (6) is employed to guarantee the accurate steady-state value for each output duty cycle.

III. Proposed Control Technique

The proposed system shown in Fig. 1 aims to be controlled through PPM. To this end, the controllability evaluation based on the small-signal models is comprehensively established at the first. Then, the required state feedback gains are designed using PPM and the proposed closed-loop control system associated with each converter will be discussed as well.

A. Controllability evaluation

The small-signal model is used to design the appropriate control techniques for the hybrid converter. Given $\tilde{x}_1 = \begin{bmatrix} \tilde{i}_{Lm} & \tilde{i}_{L2} \end{bmatrix}$ and $\tilde{x}_2 = \begin{bmatrix} \tilde{v}_{ok} & \tilde{i}_{Dok} \end{bmatrix}$ as well as $d_{m1}=d_{m2}=d_m$, the small-signal model of the hybrid converter based on the equations (1) and (3) is achieved as the following,

$$\begin{bmatrix} \dot{\tilde{x}}_1^T \\ \dot{\tilde{x}}_2^T \end{bmatrix} = \begin{bmatrix} A_1 \tilde{x}_1^T \\ A_2 \tilde{x}_2^T \end{bmatrix} + \begin{bmatrix} B_1 \tilde{d}_m \\ B_2 \tilde{d}_{ok} \end{bmatrix} + \begin{bmatrix} \tilde{S}_1 \\ \tilde{S}_2 \end{bmatrix} \tag{8}$$

Where $A_1, A_2, B_1, B_2, \tilde{S}_1$ and $\tilde{S}_2$ are equal to:

$$A_1 = \begin{bmatrix} \frac{-\left(R_1\right)}{L_1+L_m} & 0 \\ \frac{-n\left(L_m R_1\right)}{L_2\left(L_1+L_m\right)} & \frac{-R_2}{L_2} \end{bmatrix}, A_2 = \begin{bmatrix} \frac{-1}{R_{ok}C_{ok}} & \frac{D_{ok}}{C_{ok}} \\ \frac{-R_{pk}D_{ok}}{L_B} & \frac{-R_B D_{ok}}{L_B} \end{bmatrix} \tag{9}$$

$$B_1 = \begin{bmatrix} \frac{\alpha}{L_1+L_m} \\ \left(\frac{V_{Cs4}-V_c}{L_2} + \frac{nL_m\alpha}{L_2\left(L_1+L_m\right)}\right) \end{bmatrix}, B_2 = \begin{bmatrix} \frac{I_{Dok}}{C_{ok}} \\ \left(\frac{-R_B}{L_B} I_{Dok} + \frac{R_{pk}\left(D_i\left(V_{CDS}+V_{PV}\right)\right)}{L_B}\right) \end{bmatrix}$$

$$\tilde{S}_1 = \begin{bmatrix} \frac{\left(1-D_m\right)\tilde{v}_{Cs2} + D_m\tilde{v}_{AB}}{L_1+L_m} \\ \left(\frac{nL_m\left(\left(1-D_m\right)\tilde{v}_{Cs2} + D_m\tilde{v}_{AB}\right)}{L_2\left(L_1+L_m\right)} + \frac{D_m\tilde{v}_{Cs4} + \left(1-D_m\right)\tilde{v}_c}{L_2}\right) \end{bmatrix}, \tilde{S}_2 = \begin{bmatrix} 0 \\ \frac{R_{pk}D_{ok}D_i}{L_B}\left(\tilde{v}_{CDS}+\tilde{v}_{PV}\right) \end{bmatrix}$$

The small-signal term of the state variable x is driven as $\tilde{x} = X - x$ wherein X is the related steady-state term. PPM is chosen in this proposal to control the different functions of the converter shown in Fig. 1. *PPM* enables the poles of the closed-loop system to be positioned at desirable stable locations. This effective positioning of poles should be established through an appropriate designing of the state feedback gain matrix. This method can be applied to this converter if the state controllability of the system presented in (8) is guaranteed using the following matrix:

$$\phi_c = \begin{bmatrix} B_1 & A_1B_1 & B_2 & A_2B_2 \end{bmatrix} \tag{10}$$

The system controllability can be satisfied if $\left[\phi_c\right]_{1\times1} \neq 0$ and $\left[\phi_c\right]_{1\times2} \neq 0$. $\left[X\right]_{c\times d}$ stands for the element of matrix X in the c-th row and d-th column. To accurately assess the proposed system controllability, the elements $\left[\phi_c\right]_{1\times1}$ and $\left[\phi_c\right]_{1\times2}$ of the controllability matrix (10) are respectively obtained according to (11) and (12),

$$\left[\phi_c\right]_{1\times1} = \frac{\left[\begin{array}{l}\left(-L_mR_2\right)\left(nL_1+nL_m\right)\alpha \\ +\left(\left(R_1\right)\left(L_1+L_m\right)L_2 - R_2\left(L_1+L_m\right)^2\right)\left(V_{Cs4}-V_c\right)\end{array}\right]}{\left(L_2\right)^2\left(L_1+L_m\right)^3} \tag{11}$$

$$[\phi_c]_{1\times 2}=\frac{\begin{bmatrix}-L_B\left[R_{pk}D_{ok}R_{ok}+R_B\right](I_{Dok})^2+\\ \begin{bmatrix}(I_{Dok}L_B+R_BI_{Dok}D_{ok}R_{ok}C_{ok})\\ -D_{ok}R_{ok}C_{ok}R_{pk}\left(D_i\begin{pmatrix}V_{CDS}\\+V_{PV}\end{pmatrix}-V_{ok}\right)\end{bmatrix}R_{pk}\left(D_i\begin{pmatrix}V_{CDS}\\+V_{PV}\end{pmatrix}\right)\\ -V_{ok}\end{bmatrix}}{R_{ok}(L_B)^2(C_{ok})^2} \quad (12)$$

Supposing $L_mR_2 \neq 0$ and $R_2(L_1+L_m) \neq L_2(R_1)$, $[\phi_c]_{1\times 1}\neq 0$ is proved when the primary conditions $V_{Cs2} \neq V_{AB}$ and $V_{Cs4} \neq V_c$ are satisfied by preventing the concurrent turn-on of the switches (M_1,M_2) and (M_3,M_4) through the proposed control system.

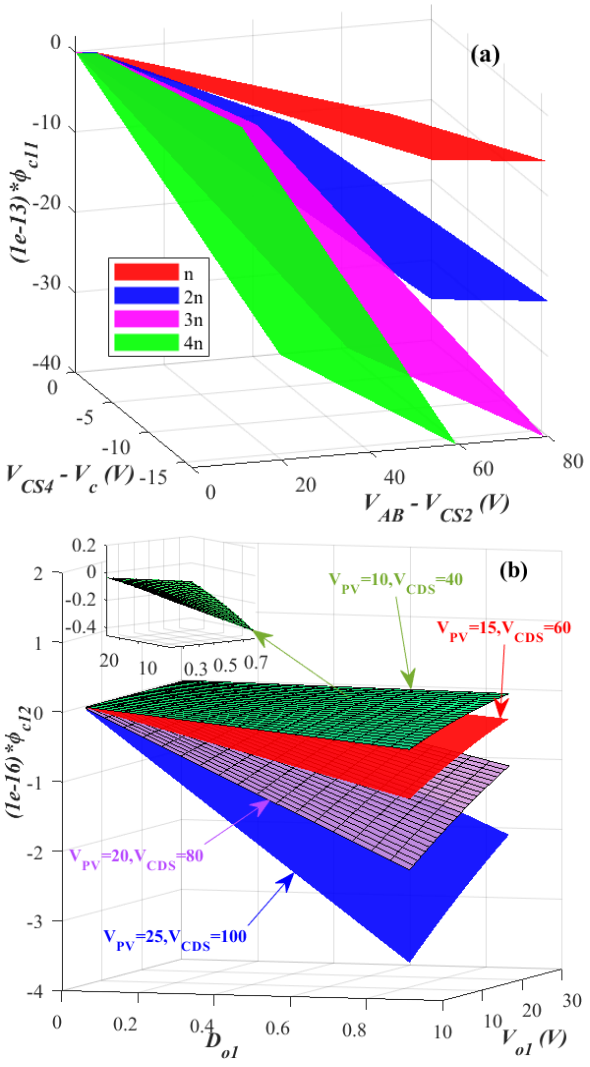

Fig. 3. (a) Alteration of the element $[\phi_c]_{1\times 1}$ based on (V_{CS4} - V_c) and (V_{AB} - V_{CS2}) when the transformer ratio (n) increases, and (b) alteration of the element $[\phi_c]_{1\times 2}$ based on D_{o1} and V_{o1} with different values of V_{PV} and V_{CDS}.

To further assessment, Fig. 3(a) and (b) are respectively plotted using (11) and (12) to detail the variation trend of the controllability matrix elements. Based on Fig. 3(a), given the different values for (V_{CS4} - V_c) and (V_{AB} - V_{CS2}), the element $[\phi_c]_{1\times 1}$ is getting much far from the zero value as the transfer ratio increases. Also, the three-dimension curve of $[\phi_c]_{1\times 2}$ based on D_{o1} and V_{o1} is illustrated in Fig. 3(b). Based on this figure, the element $[\phi_c]_{1\times 2}$ will never reach zero value even as V_{PV} and V_{CDS} are assigned to different voltage levels.

A. Closed-loop control system

Well-designed state feedback gains can lead to an effective PPM for controlling the proposed system shown in Fig. 1. In this paper, the feedback matrix K_F in (13) is presented through considering the state gains for both *ACBFC* and SISIMO DC/DC buck converter.

$$K_F=\begin{bmatrix}k_{p1}+\dfrac{k_{i1}}{s} & k_{p2}+\dfrac{k_{i2}}{s}\\ k_{p3}+\dfrac{k_{i3}}{s} & 0\end{bmatrix} \quad (13)$$

Defining $K_{F1}=\begin{bmatrix}[K_F]_{1\times 1} & [K_F]_{1\times 2}\end{bmatrix}$ and $K_{F2}=\begin{bmatrix}[K_F]_{2\times 1} & [K_F]_{2\times 2}\end{bmatrix}$ as the feedback gains for respectively *ACBFC* and the buck converter, the proposed duty cycles equalize $\tilde{d}_m=-K_{F1}\tilde{x}_1^T$ and $\tilde{d}_{ok}=-K_{F2}\tilde{x}_2^T$. State feedback K_{F1} is employed to control the current flow of *ACBFC* in all three operation modes. In the proposed control system designed for *ACBFC*, the relationships $\tilde{i}_{L2}=k_{L2}\tilde{i}_{Lm}$ and $\tilde{i}_{Lm}=k_{Lm}\tilde{i}_{L2}$ are applied. Therefore, given the aforesaid explanations as well as the dynamic models of (1) and (8), the proposed closed-loop control system for *ACBFC* is obtained in accordance with Fig. 4(a) resulting in the new matrix of $B_1'=B_1K_{F1}$ represented by (14). In addition, based on the dynamic equations of (3) and (8) as well as using the state feedback K_{F2} used for controlling the voltages of SISIMO buck DC/DC converter, the closed-loop control system for LVLs is proposed as illustrated in Fig. 4(b). Focusing on the lately closed-loop system, the new matrix of $B_2'=B_2K_{F2}$ will be equal to (15).

$$B_1'=\begin{bmatrix}\left(\dfrac{\alpha}{L_1+L_m}\right)\begin{pmatrix}[K_F]_{1\times 1}\\+k_{L2}[K_F]_{1\times 2}\end{pmatrix} & 0\\ 0 & \begin{pmatrix}\dfrac{V_{Cs4}-V_c}{L_2}\\+\dfrac{nL_m\alpha}{L_2(L_1+L_m)}\end{pmatrix}\begin{pmatrix}k_{Lm}[K_F]_{1\times 1}\\+[K_F]_{1\times 2}\end{pmatrix}\end{bmatrix} \quad (14)$$

$$B_2'=\begin{bmatrix}\left(\dfrac{I_{Dok}}{C_{ok}}\right)[K_F]_{2\times 1} & 0\\ \begin{pmatrix}\dfrac{-R_B}{L_B}I_{Dok}+\\ \dfrac{R_{pk}\left(D_i(V_{CDS}+V_{PV})-V_{ok}\right)}{L_B}\end{pmatrix}[K_F]_{2\times 1} & 0\end{bmatrix} \quad (15)$$

In the proposed *PPM*, the values of the feedback gains k_{pi} and k_{ii} (i=1,2,3) should be chosen so that the eigenvalues of the matrix "$sI-A_j+B'_j$" ($j=1,2$) can be effectively stable. The eigenvalues of the *ACBFC* closed-loop system are achieved by satisfying the relationship "$sI-A_1+B'_1=0$" as illustrated in Fig. 5(a). This figure includes from only large real parts to all complex values with negative real components.

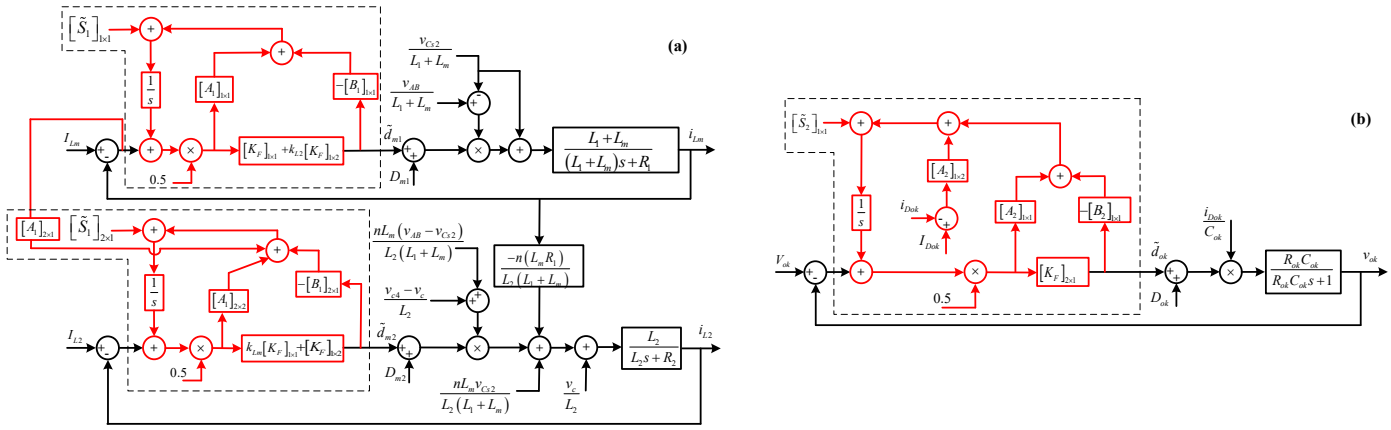

Fig. 4. Closed-loop control system for (a) *ACBFC*, and (b) *SISIMO* buck DC/DC converter.

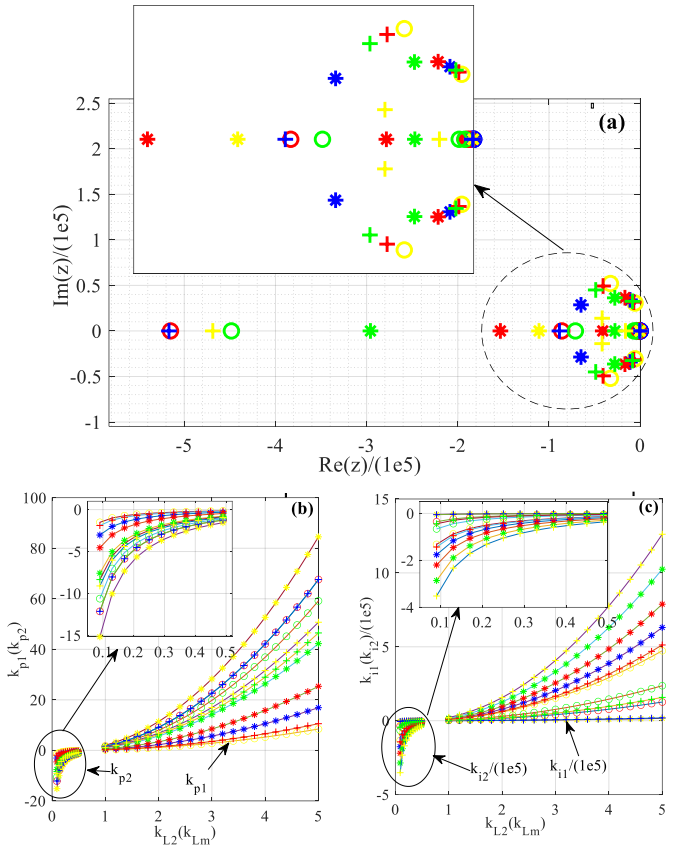

Fig. 5. (a) Eigenvalues of *ACBFC* closed-loop system, (b) the proportional coefficients of k_{p1} and k_{p2} with different k_{L2} and k_{Lm}, and (c) the integral coefficients of k_{i1} and k_{i2} with different k_{L2} and k_{Lm}.

The open-loop eigenvalues (zero feedback gains) for *ACBFC* are equal to s = -666.667, -74.259, 0, and 0. In this paper, the *ACBFC* closed-loop eigenvalues are chosen as the following:

$$eig\left(sI - A_1 + B_1'\right) = \left(-41.703.796 \pm 13.9336i\right)\times 10^3, \; -468.695\times 10^3, -16.099\times 10^3 \quad (16)$$

Comparing the open-loop eigenvalues with the eigenvalues presented in Fig. 5(a), it can be realized that more effective control coefficients commensurate with stable eigenvalues with large stability margins can be driven based on proposed closed-loop control systems. Using a wide range of stable eigenvalues and allowable approximate values for ratio i_{Lm}/i_{L2}, the proportional and integral coefficients of $k_{p(i)1}$ and $k_{p(i)2}$ versus different values of k_{L2} and k_{Lm} are plotted according to Fig. 5(b) and 5(c), respectively. Considering the eigenvalues of (16) as well as the control coefficients in Fig. 5(b) and 5(c), the *ACBFC* control coefficients are achieved as (17) that will be applied to Fig. 4(a),

$$place\left(A_1, B_1, K_{F1}, B_1', \hat{\gamma}\right) = \begin{bmatrix} k_{p1} & k_{i1} \end{bmatrix} = \begin{bmatrix} 23.7150 & 5.7721\times 10^5 \end{bmatrix} \quad (17)$$
$$\begin{bmatrix} k_{p2} & k_{i2} \end{bmatrix} = \begin{bmatrix} -2.16 & -8.352\times 10^4 \end{bmatrix}$$

Using (9) and (15), the eigenvalues of SISIMO buck DC/DC converter will be assessed based on the relationship "sI-A_2+B'_2=0". This relationship is employed as well to achieve the open-loop eigenvalues of the buck converter for both voltages of v_{o1} and v_{o2} that are s = {-452.393, -1.35, 0} and {-987.5, -10.57, 0}, respectively. It aims to achieve the closed-loop eigenvalues of the buck converter output voltages as follows:

$$eig\left(sI - A_2 + B_2'\right)\Big|_{v_{o1}} = \left(-99.072 \pm 3.11i\right)\times 10^3, -100.049 \quad (18)$$

$$eig\left(sI - A_2 + B_2'\right)\Big|_{v_{o2}} = \left(-122.993 \pm 15.316i\right)\times 10^3, -469.5 \quad (19)$$

The eigenvalues presented in (18) and (19) will result in the [k_{p3}, k_{i3}] equal to [0.01, 50×10^3] and [0.04, 100×10^3] for the output voltages of v_{o1} and v_{o2}, respectively.

IV. Simulation and Experimental Results

Both simulation and experimental results are presented to validate the operation of proposed APM and BMS system under the designed closed-loop controller. To this end, MATLAB/SIMULINK environment is employed to analyze the dynamic operation of proposed system when a variable PV power profile is applied as illustrated in Fig. 6. As shown in Fig. 6(a), the LVAB appropriately utilizes its power to charge the EV-HVBC while also supplying the remaining power demand of the two LVLs that cannot be provided by the PV unit. Based on this figure, the state-of-charge (SOC) profiles of the LVAB and EV-HVBC demonstrate that the proposed system can effectively manage both discharging and charging processes.

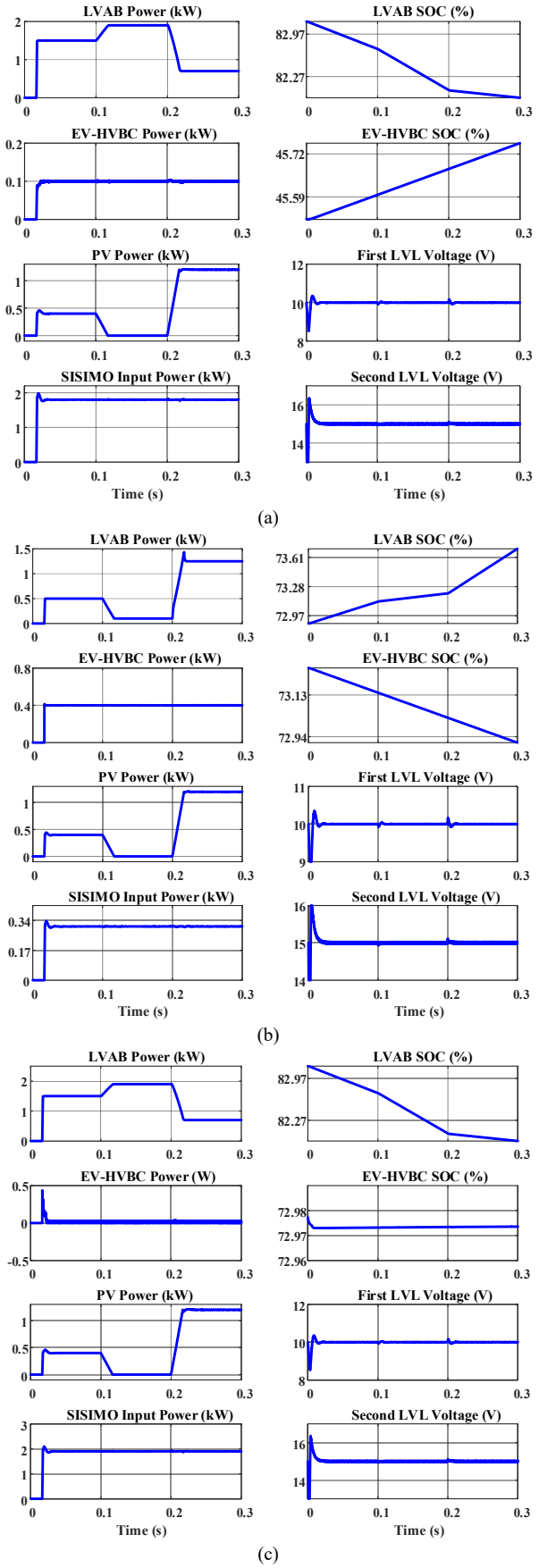

Fig. 6. Dynamic operation of proposed PV-integrated APM and EV BMS when a variable PV power profile is applied for (a) OM-I, (b) OM-II, and (c) OM-III.

Meanwhile, the LVL voltages are maintained at their reference values with satisfactory steady-state and dynamic performance. As shown in Fig. 6(b), the EV-HVBC is effectively discharged to charge the LVAB while supplying the LVLs in coordination with the PV unit. Due to the limited power available from the EV-HVBC, the operation of the proposed system can be switched from OM-II to OM-III to supply the required power to the LVLs. In OM-III, the EV-HVBC is neither charged nor discharged, while the LVAB, in coordination with the PV unit, supplies the LVLs. As shown in Fig. 6(c), the SOC of the LVAB gradually decreases, whereas the SOC of the EV-HVBC remains unchanged in this operating mode. In this operation mode, given the smooth input power for SISIMO converter, the proposed APM and BMS system with its closed-loop controller can provide desirable voltages for LVLs as depicted in Fig. 6(c).

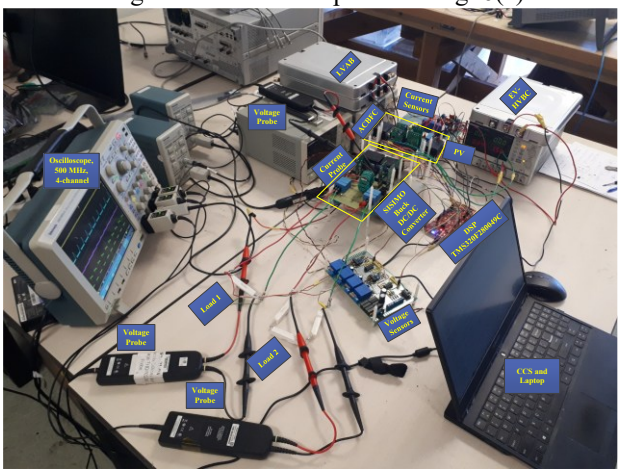

Fig. 7. The experimental setup of proposed PV-integrated APM and EV-BMS.

Table II: Experimental parameters.

Parameter	Value	Parameter	Value
SISIMO buck DC/DC converter inductance, L_B (H)	78µ	*Output capacitor for first load, C_{o1} (F)*	47µ
SISIMO buck DC/DC converter resistor, R_B (Ω)	0.035	*Output capacitor for first load, C_{o2} (F)*	22µ
First load resistor, R_{o1} (Ω)	47	*Transformer ratio, $n=n_2/n_1$*	4/14
Second load resistor, R_{o2} (Ω)	4.6	*PV voltage, v_{PV}* (V)	10
Resistor commensurate with i_{Do1}, R_{p1} (Ω)	0.091	*LVAB voltage, v_{AB}* (V)	14
Resistor commensurate with i_{Do2}, R_{p2} (Ω)	0.909	*EV battery cell voltage, v_c* (V)	4
Primary side leakage inductance, L_1 (H)	4µ	*Secondary side transformer resistor, R_2* (Ω)	1m
Secondary side leakage inductance, L_2 (H)	1.5µ	*Magnetizing inductance, L_m* (H)	50µ
Primary side transformer resistor, R_1 (Ω)	4m		

The performance of the proposed PV-integrated APM with two LVLs is also evaluated using the experimental prototype as shown in Fig. 7. To this end, DSP TMS320F280049C is employed to generate the signals required for the MOSFETs IPP023N08N5 (used for M_1-M_4, M_i, M_{o1}, and M_{o2}) with the switching frequency 120 kHz. As can be seen from Fig. 7, the battery cells of Nickel Manganese Cobalt (NMC) Nissan Leaf Gen. 3 with the specifications presented in Table II are utilized for making the ALVB and EV-HVBC in the proposed APM

system. In addition, a 10V DC power supply is considered to emulate the PV unit. Other parameters of the experimental prototype are given in Table II.

A. Steady-state responses

Fig. 8(a), (b) and (c) illustrate the steady-state experimental results for OM-I, OM-II, and OM-III, respectively. Two resistive loads with the same value of 31 Ohms are connected to both outputs. According to Figs. 8(a)-8(c), the input voltage of the SISIMO buck DC/DC converter (i.e., v_{PV} + v_{CDS}) is changed commensurately with the chosen operation mode. Using the proposed control technique, at each operation mode, the same voltage is achieved for both output loads in presence of distinct input voltages, and the current of the inductor L_B is flowed accordingly. Comparing the steady-state responses of three operation modes in Fig. 8, because of larger voltage magnitude associated with the voltage v_{DS1} in *ACBFC*, the larger input voltage is created for the SISIMO buck DC/DC converter at OM-I. As was expected, according to Fig. 8(a)-(c), the largest and smallest inductor current have respectively belonged to OM-I and OM-III.

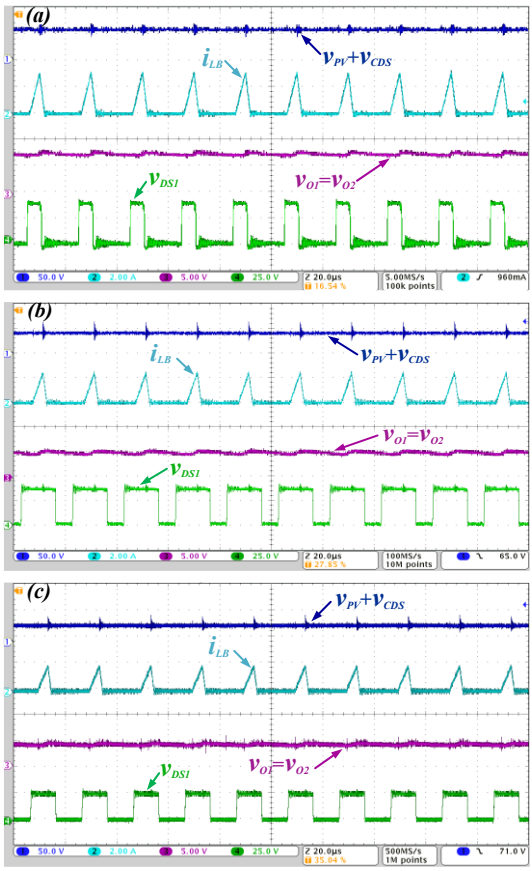

Fig. 8. Steady-state experimental results for (a) OM-I, (b) OM-II, and (c) OM-III.

B. Dynamic responses

In this section, the dynamic responses in two operation modes of OM-II and OM-III are investigated. The dynamic experimental results in OM-II due to the input voltage variation of the SISIMO buck DC/DC converter are presented in Fig. 9(a)-9(d) along with taking the zoom-in results into account as well. Fig. 9(a) illustrates v_{DS1}, i_{LB}, -i_c, and i_{PV} before/during the input voltage change and after compensation. As can be seen from this figure, the currents of inductor L_B, EV-HVBC, and PV panel experience a rise while the input voltage changes owing to an unpredictable perturbation into the duty cycle of d_m.

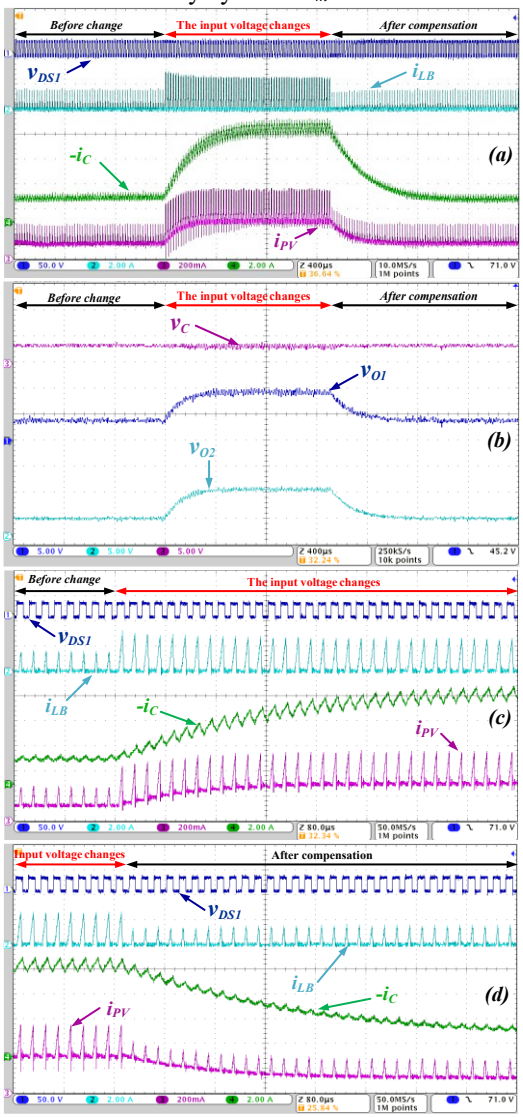

Fig. 9. Dynamic experimental results for OM-II while the input voltage of the SISIMO buck DC/DC converter changes, (a) v_{DS1}, i_{LB}, -i_c, and i_{PV} before/during the input voltage change and after compensation, (b) v_c, v_{o1}, and v_{o2} before/during the input voltage change and after compensation, (c) (Zoom-in) v_{DS1}, i_{LB}, -i_c, and i_{PV} before/during the input voltage change, and (d) (Zoom-in) v_{DS1}, i_{LB}, -i_c, and i_{PV} during the input voltage change and after compensation.

It is worth mentioning that the increment of the currents during the disturbed duty cycle are caused through the increasing values of the load voltages v_{o1} and v_{o2} according to Fig. 9(b). Based on this figure, the cell voltage is somewhat fluctuated during the input voltage variation as well. The zoom-in experimental results of {v_{DS1}, i_{LB}, -i_c, i_{PV}} before/during and during/after the input voltage variation are depicted in Fig. 9(c) and 9(d), respectively. In this dynamic result scenario, when the proposed control technique starts compensating the duty cycle perturbation, all the currents of i_{LB}, -i_c, and i_{PV} as well as the load voltages (v_{o1} and v_{o2}) move toward (and reach) their desirable values with very good

dynamic response and minimum steady-state error as can be realized from Figs. 9(a), 9(b), and 9(d). In this dynamic response analysis, it also shows that the EV-HVBC is successfully capable of accomplishing the generation process of discharging current using the proposed control technique to appropriately charge the LVAB and supply the remaining current of LVLs while the PV is supplying the loads as well.

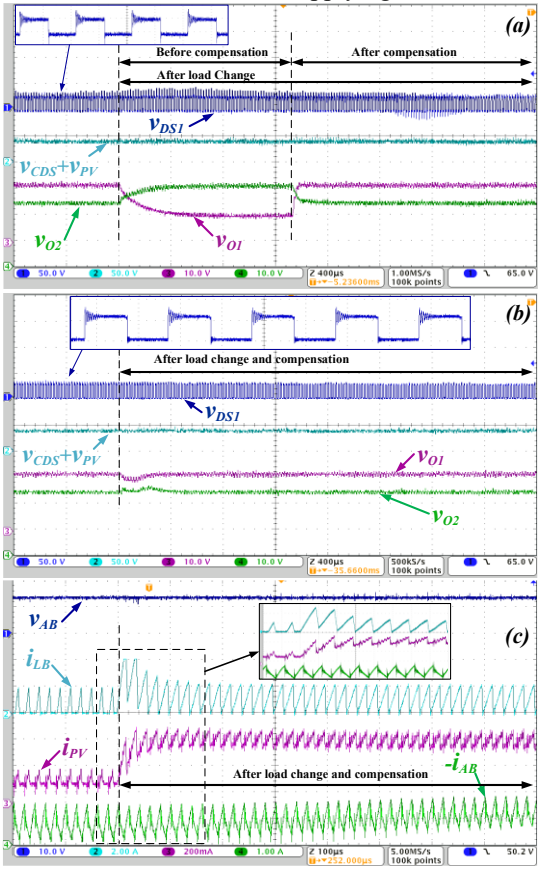

Fig. 10. Dynamic experimental results for OM-III while sudden LVLs change occurs, (a) v_{DS1}, v_{CDS} + v_{PV}, v_{o1}, and v_{o2} before load change/compensation and after load change/compensation, (b) (Zoom in) v_{DS1}, v_{CDS} + v_{PV}, v_{o1}, and v_{o2} after load change and compensation, and (c) (Zoom-in) v_{AB}, i_{LB}, i_{PV}, and -i_{AB} after load change and compensation.

Fig. 10 indicates the dynamic experimental results of {v_{DS1}, v_{CDS} + v_{PV}, v_{o1}, v_{o2}} and {v_{AB}, i_{LB}, i_{PV}, -i_{AB}} for OM-III while sudden LVLs variation occurs. Fig. 10(a) shows that to what extent the LVLs voltages can be adversely affected if the proposed control technique does not compensate for the LVLs variations. According to this figure, when the proposed controller starts compensating for the LVLs variation, the voltages v_{o1} and v_{o2} appropriately approach to their reference values with very fast dynamic reaction. Fig. 10(b) concentrates on the LVLs variation compensation right away after the LVLs changes. As can be realized from this figure, relying on the proposed control technique, the LVLs voltages can keep going to their desirable values with acceptable over/undershoots and approximately no steady-state error. The dynamic results of the currents of inductor L_B, PV panel, and LVAB are shown in Fig. 10(c) when the LVLs are changed and instantly compensated. This figure can ascertain whether very suitable steady-state and dynamic responses can be achieved for the currents in this operation scenario. The efficiencies of the proposed system in all three operation modes, obtained from simulation results (SOMI, SOMII, and SOMIII) and experimental results (EOMI, EOMII, and EOMIII), are presented in Fig. 11(a)–11(c). As observed from these figures, peak efficiencies of 95.2% and 94.5% are achieved for the proposed PV-integrated APM and EV BMS system in the simulation and experimental results, respectively.

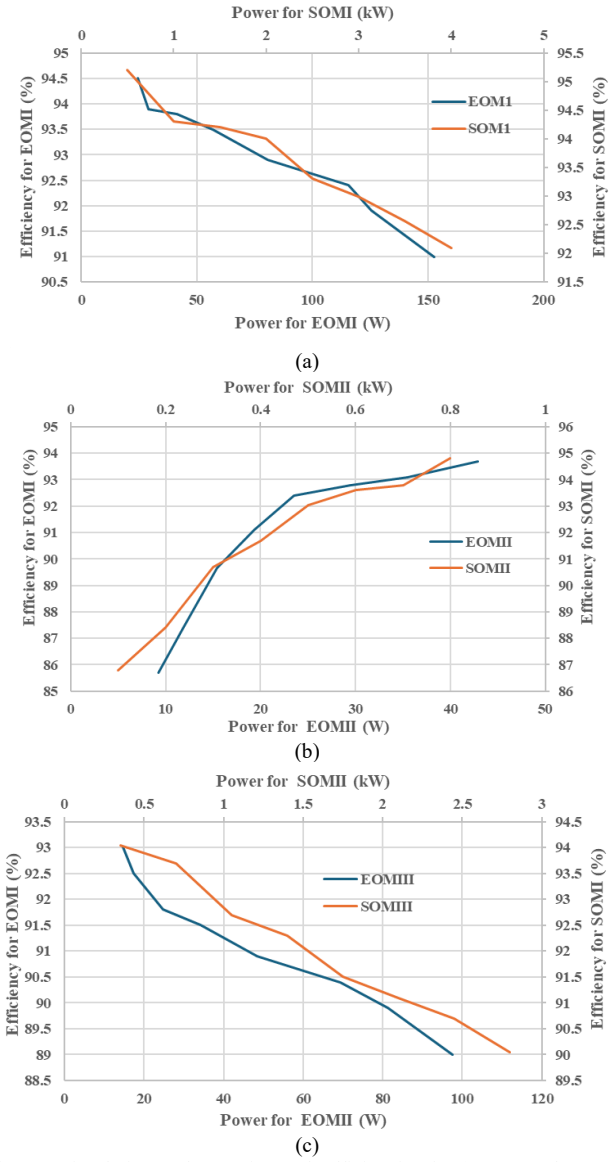

Fig. 11. Simulation and Experimental Efficiencies for (a) OM1, (b) OM2, and (c) OM3.

V. Conclusion

A hybrid multi-port DC-DC converter has been proposed in this paper to integrate PV unit and APM for supplying the EV-low voltage/power loads and actively participating in EV-BMS at the same time. Using ACBFC and SISIMO buck DC/DC converter, the proposed converter guaranteed multiple outputs isolated from EV-HVB with significant safe operation modes including charging, discharging and idle resulting in different power flow directions between the auxiliary battery and EV battery cell. Using comprehensive large-signal and

small-signal dynamic models of the proposed converter, two closed-loop control systems based on PPM have been presented to provide the desirable current flow and regulated output voltages in different operating conditions. In this regard, the controllability of the proposed system has been extensively assessed, and the effective state feedback gains have been designed by focusing on the closed-loop system eigenvalues with the adjusted and sufficient stability margin. Compared to the existing APMs, the proposed PV-integrated APM is capable of providing much wider voltage ranges for internal loads through LVAB with a smaller voltage rate and size. Simulation and experimental results along with efficiency evaluations have verified that the proposed system with its designed control techniques can make noticeable contributions to the APM and BMS in EV applications.

REFERENCES

[1] C. Wang, P. Zheng and J. Bauman, "A Review of Electric Vehicle Auxiliary Power Modules: Challenges, Topologies, and Future Trends," IEEE Transactions on Power Electronics, vol. 38, no. 9, pp. 11233-11244, Sept. 2023.

[2] R. Hou and A. Emadi, "A Primary Full-Integrated Active Filter Auxiliary Power Module in Electrified Vehicles with Single-Phase Onboard Chargers," IEEE Transactions on Power Electronics, vol. 32, no. 11, pp. 8393-8405, Nov. 2017.

[3] H. -P. Kieu, D. B. -H. Nguyen and S. Choi, "An All-in-one Magnetic Structure for Entire ZVS Range Auxiliary Power Module in Electrical Vehicles," IEEE Transactions on Power Electronics, Early Access.

[4] A. M. Naradhipa, S. Kim, D. Yang, S. Choi, I. Yeo and Y. Lee, "Power Density Optimization of 700 kHz GaN-Based Auxiliary Power Module for Electric Vehicles," IEEE Transactions on Power Electronics, vol. 36, no. 5, pp. 5610-5621, May 2021.

[5] Y. Bi et al., "An Integrated Power Decoupling Method for Single-Phase EV Onboard Charger in V2G Application," IEEE Transactions on Power Electronics, vol. 38, no. 8, pp. 9635-9646, Aug. 2023.

[6] R. Hou and A. Emadi, "Applied Integrated Active Filter Auxiliary Power Module for Electrified Vehicles with Single-Phase Onboard Chargers," IEEE Transactions on Power Electronics, vol. 32, no. 3, pp. 1860-1871, March 2017.

[7] L. Zhu, H. Bai, A. Brown and M. McAmmond, "Design a 400 V–12 V 6 kW Bidirectional Auxiliary Power Module for Electric or Autonomous Vehicles with Fast Precharge Dynamics and Zero DC-Bias Current," IEEE Transactions on Power Electronics, vol. 36, no. 5, pp. 5323-5335, May 2021.

[8] L. Zhu, H. Bai and A. Brown, "Model and Control of a Current-Fed Dual Active Bridge Based Ultrawide-Voltage-Range Auxiliary Power Module for 400 V/800 V Electric Vehicles," IEEE Transactions on Power Electronics, vol. 39, no. 3, pp. 3263-3276, March 2024.

[9] S. Kim and F. -S. Kang, "Multifunctional Onboard Battery Charger for Plug-in Electric Vehicles," IEEE Transactions on Industrial Electronics, vol. 62, no. 6, pp. 3460-3472, June 2015.

[10] Y. Wu, H. Wang, Y. Zhuang and Y. Zhang, "A Shared Charging Channel for Power and Auxiliary Batteries in Electric Vehicles," IEEE Transactions on Industrial Electronics, vol. 71, no. 7, pp. 8202-8206, July 2024.

[11] A. Avila, A. Garcia-Bediaga, I. Alzuguren, M. Vasić and A. Rujas, "A Modular Multifunction Power Converter Based on a Multiwinding Flyback Transformer for EV Application," IEEE Transactions on Transportation Electrification, vol. 8, no. 1, pp. 168-179, March 2022.

[12] Y. Zhang et al., "An Integrated Electric Vehicle Charging System of Wireless Power Transfer and Auxiliary Power Module with Shared Converter and Magnetic Coupler," IEEE Transactions on Industrial Electronics, vol. 71, no. 9, pp. 10414-10421, Sept. 2024.

[13] Z. Liang et al., "Full Integration of On-Board Charger, Auxiliary Power Module, and Wireless Charger for Electric Vehicles Using Multipurpose Magnetic Couplers," IEEE Transactions on Industrial Electronics, vol. 71, no. 8, pp. 9962-9967, Aug. 2024.

[14] I. Kougioulis, A. Pal, P. Wheeler and M. R. Ahmed, "An Isolated Multiport DC–DC Converter for Integrated Electric Vehicle On-Board Charger," IEEE Journal of Emerging and Selected Topics in Power Electronics, vol. 11, no. 4, pp. 4178-4198, Aug. 2023.

[15] N. Tashakor, J. Kacetl, D. Keshavarzi and S. Goetz, "Topology, Analysis, and Modulation Strategy of a Fully Controlled Modular Reconfigurable DC Battery Pack with Interconnected Output Ports for Electric Vehicles," IEEE Transactions on Transportation Electrification, vol. 10, no. 1, pp. 1180-1193, March 2024.

[16] M. Preindl, "A Battery Balancing Auxiliary Power Module with Predictive Control for Electrified Transportation," IEEE Transactions on Industrial Electronics, vol. 65, no. 8, pp. 6552-6559, Aug. 2018.

[17]W. Wang and M. Preindl, "Dual Cell Links for Battery-Balancing Auxiliary Power Modules: A Cost-Effective Increase of Accessible Pack Capacity," IEEE Transactions on Industry Applications, vol. 56, no. 2, pp. 1752-1765, March-April 2020.

[18] W. Wang, Y. A. Fahmy and M. Preindl, "A Low-Cost Battery-Balancing Auxiliary Power Module with Dual-Active Half Bridge Links and Coreless Transformers," IEEE Transactions on Transportation Electrification, vol. 9, no. 3, pp. 3801-3809, Sept. 2023.

[19] M. Evzelman, M. M. Ur Rehman, K. Hathaway, R. Zane, D. Costinett and D. Maksimovic, "Active Balancing System for Electric Vehicles with Incorporated Low-Voltage Bus," IEEE Transactions on Power Electronics, vol. 31, no. 11, pp. 7887-7895, Nov. 2016.

[20] M. Dhananjaya, D. Potnuru, P. Manoharan and H. H. Alhelou, "Design and Implementation of Single-Input-Multi-Output DC-DC Converter Topology for Auxiliary Power Modules of Electric Vehicle," IEEE Access, vol. 10, pp. 76975-76989, 2022.

[21] G. Chen, Y. Deng, J. Dong, Y. Hu, L. Jiang and X. He, "Integrated Multiple-Output Synchronous Buck Converter for Electric Vehicle Power Supply," IEEE Transactions on Vehicular Technology, vol. 66, no. 7, pp. 5752-5761, July 2017.

[22] T. Kim and S. Kwak, "A Flexible Voltage Bus Converter for the 48-/12-V Dual Supply System in Electrified Vehicles," IEEE Transactions on Vehicular Technology, vol. 66, no. 3, pp. 2010-2018, March 2017.

[23] T. Jalilzadeh, N. Rostami, E. Babaei and S. H. Hosseini, "Multiport DC–DC Converter with Step-Up Capability and Reduced Voltage Stress on Switches/Diodes," IEEE Transactions on Power Electronics, vol. 35, no. 11, pp. 11902-11915, Nov. 2020.

[24] M. Dhananjaya, D. Ponuru, T. S. Babu, B. Aljafari and H. H. Alhelou, "A New Multi-Output DC-DC Converter for Electric Vehicle Application," IEEE Access, vol. 10, pp. 19072-19082, 2022.

[25] Lambert, F., “Tesla Cybertruck Will Have Solar Roof Option to Add 15 Miles of Range per Day,” www.electrek.com, accessed 13 Jun 2020.

[26] Illia Diahovchenko, Lubov Petrichenko, Ihor Borzenkov, Michal Kolcun, "Application of photovoltaic panels in electric vehicles to enhance the range," Heliyon, Volume 8, Issue 12, 2022, e12425.

[27] M. Yamaguchi et al., “Analysis for expansion of driving distance and CO2 emission reduction of photovoltaic-powered vehicles,” IEEE J. Photovolt., vol. 13, no. 3, pp. 343–348, May 2023.

[28] M. H. Mobarak, R. N. Kleiman, and J. Bauman, “Solar-charged electric vehicles: A comprehensive analysis of grid, driver, and environmental benefits,” IEEE Trans. Transport. Electrific., vol. 7, no. 2, pp. 579–603, Jun. 2021.

[29] L. Zhang, F. Luo, and T. Hossein Rashidi, “Route planning of photovoltaic-integrated urban waste collection vehicles,” IEEE Trans. Transport. Electrific., vol. 11, no. 2, pp. 6490–6501, Apr. 2025.

[30] M. Yamaguchi et al., “Analysis for effects of temperature rise of PV modules upon driving distance of vehicle integrated photovoltaic electric vehicles,” Energy Power Eng., vol. 16, no. 4, pp. 131–150, 2024.

[31] M. Yamaguchi et al., “Importance of developing high-efficiency solar cells for PV-powered vehicles,” in Proc. 47th IEEE Photovoltaic Spec. Conf. (PVSC), Jun. 2020, pp. 0221–0223.

[32] Bi Li, Zhinong Li, Deqiang He, "Research and optimization of energy management system for photovoltaic vehicles," Energy, Volume 289, 2024, 129776.

[33] Hongqian Wei, Yan Zhong, Likang Fan, Qiang Ai, Wenqiang Zhao, Rui Jing, Youtong Zhang, "Design and validation of a battery management system for solar-assisted electric vehicles," Journal of Power Sources, Volume 513, 2021, 230531.

[34] Yiyang Peng, Zhuowei Wang, Anthony Chen, "Benefiting from solar: Optimal scheduling for solar electric buses with onboard PV auxiliary power," Applied Energy, Volume 408, 2026, pp. 127360.

[35] Zhou Jin, Dongyang Li, Daning Hao, Zutao Zhang, Liang Guo, Xiaoping Wu, Yanping Yuan, “A portable, auxiliary photovoltaic power system for electric vehicles based on a foldable scissors mechanism,” Energy and

Built Environment, Volume 5, Issue 1, 2024, Pages 81-96, ISSN 2666-1233, https://doi.org/10.1016/j.enbenv.2022.08.002.

[36] C. Duan et al., "A Solar Power-Assisted Battery Balancing System for Electric Vehicles," IEEE Transactions on Transportation Electrification, vol. 4, no. 2, pp. 432-443, June 2018.

[37] Chen Duan, Zhongyang Zhao, Caisheng Wang, Jianfei Chen, and Matt Liao "An Electric Vehicle Onboard Microgrid with Solar Panel for Battery Module Balancing and Vehicle-to-Grid Applications", 2021 SAE International, pp. 1-10, doi:10.4271/14-10-02-0011.

[38] M. Abdelhamid, K. Rhodes, E. Christen and D. Kok., "Solar Panels on Electrified Vehicles: Applications and Off-Cycle CO2 Credit," SAE International Journal of Alternative Powertrains, Vol. 7, No. 3, WCX18, Best Papers Special Issue (2018), pp. 311-322.

[39] R. K. Shukla, D. Saha and B. G. Fernandes, "A Multifunctional Current-Fed Quad-Active Bridge Converter for On-Board Charging and Auxiliary Power in HESS-Based EVs," IECON 2025 – 51st Annual Conference of the IEEE Industrial Electronics Society, Madrid, Spain, 2025, pp. 1-6.

[40] H. Yavasoglu, B. Shani, A. Hasnain, B. Parlak and A. Khaligh, "Analysis and System Design Optimization of PV Panel and Auxiliary Battery Integration for VIPV Electric Vehicles," IEEE Transactions on Transportation Electrification, vol. 11, no. 6, pp. 13535-13545, Dec. 2025.

[41] H. Fathabadi, "Plug-In Hybrid Electric Vehicles: Replacing Internal Combustion Engine With Clean and Renewable Energy Based Auxiliary Power Sources," IEEE Transactions on Power Electronics, vol. 33, no. 11, pp. 9611-9618, Nov. 2018.

[42] Yun-Kyung Hwang1 and Kwang-Hee Nam, "A PV-Module Integrated Phase Shift Full Bridge Converter for EV," The Transactions of the Korean Institute of Power Electronics, Vol. 25, No. 6, December 2020.

[43] S. R. Khasim, C. Dhanamjayulu and S. M. Muyeen, "A Single Inductor Multi-Port Power Converter for Electric Vehicle Applications," IEEE Access, vol. 11, pp. 3367-3385, 2023.

Majid Mehrasa received his PhD from University of Beira Interior (UBI), Covilha, Portugal, in 2019. During last 16 years, he persistently worked on different projects in Power Electronics, Power Electronic Applications, and Power Systems in various countries including IRAN, Portugal, Italy, France, and USA. As a Postdoctoral Research Fellow, He was involved with the industry-based projects in different universities such as University of Trieste (Italy), University of Grenoble, Alpes (G2Elab, France), University of North Dakota (EERC, USA), San Diego State University (USA), and California State University (Sacramento, USA). He is currently assistant professor at The University of New Orleans (UNO), New Orleans, USA. He has authored more than 120 articles including scholarly book chapter, refereed-journal articles and conference papers. Dr. Mehrasa is Senior Member of the IEEE. His research interests include power electronics (PEs) with its applications and related control systems, developing Artificial Intelligent (AI) for the Cybersecurity and stability enhancement of PEs-based low-inertia power systems, and Electric Vehicles.

Naser Vosoughi Kurdkandi (Member, IEEE) received the Ph.D. degree in electrical engineering and power electronics from the University of Tabriz,Tabriz, Iran, in 2019. From 2019 to 2020, he was a Postdoctoral Researcher with the University of Tabriz. In 2020, he was with Tallinn University of Technology (TalTech), Tallinn, Estonia, as a Postdoctoral Researcher. Since 2022, he has been a Postdoctoral Research Fellow with San Diego State University, San Diego, CA, USA. Since 2021, he has been recognized as one of the world's top 2% most-cited scientists, according to a global citation-based ranking by Stanford University. His research interests include multilevel inverters, grid-connected PV inverters, dc–dc switched-capacitor and switched inductor converters, fast charging stations for electric vehicles, battery-based energy storage systems, and induction motor drives.

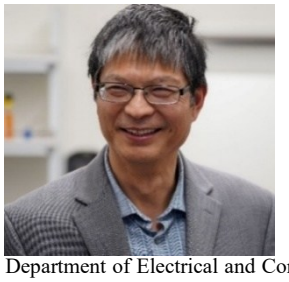

Chris Mi (Fellow, IEEE and Fellow, SAE) received the B.S.E.E. and M.S.E.E. degrees in electrical engineering from Northwestern Polytechnical University, Xi'an, China, and the Ph.D. degree in electrical engineering from the University of Toronto, Toronto, Ontario, Canada, in 1985, 1988, and 2001, respectively.

He is a Distinguished Professor in the Department of Electrical and Computer Engineering and the Director of Caili and Daniel Chang Center of Electrical Drive Transportation, San Diego State University (SDSU), San Diego, USA. Prior to joining SDSU, he was with the University of Michigan, Dearborn, from 2001 to 2015. His research interests include electric drives, power electronics, electric machines, electrical and hybrid vehicles, wireless power transfer, and power electronics.

In 2019, he received the Inaugural IEEE Power Electronics Emerging Technology Award. In 2022, he received the Albert W. Johnson Research Lectureship and was named the Distinguished Professor, the highest honor given to an SDSU faculty member, and only one award is given each year. In 2023, he received the IEEE PELS Vehicle and Transportation Systems Achievement Award, the IEEE Transactions on Industry Applications Best Paper Award, and the SDSU Innovator of the Year Award. In 2024, he received the prestigious Alumni Distinguished Faculty Award from SDSU. Most recently, he received the Wang Family Excellence Award from the California State University System.